Influenza infection induces host DNA damage and dynamic DNA damage responses during tissue regeneration

Citation: Li, Na et al. "Influenza Infection Induces Host DNA Damage and Dynamic DNA Damage Responses during Tissue Regeneration." Cellular and Molecular Life Sciences 72.15 (2015): 2973–2988.

As Published: http://dx.doi.org/10.1007/s00018-015-1879-1

Publisher: Springer Basel

Persistent URL: http://hdl.handle.net/1721.1/103152

Version: Author's final manuscript: final author's manuscript post peer review, without publisher's formatting or copy editing

Influenza infection induces host DNA damage and dynamic DNA damage responses during tissue regeneration

Na Li[1,3], Marcus Parrish[2], Tze Khee Chan[1,4], Lu Yin[1], Prashant Rai[1,3], Yamada Yoshiyuki[1], Nona Abolhassani[2], Kong Bing Tan[5], Orsolya Kiraly[1], Vincent TK Chow[3], Bevin P. Engelward[2]#

1 Singapore-MIT Alliance for Research and Technology

Address: 1 CREATE Way, #03-10/11 Innovation Wing; #03-12/13/14 Enterprise Wing, Singapore 138602

2 Department of Biological Engineering, Massachusetts Institute of Technology

Address: 16-743, Massachusetts Institute of Technology, 77 Massachusetts Ave., Cambridge, MA 02139. Phone: (617) 258-0260. Fax: (617) 258-0499.

3 Department of Microbiology, National University of Singapore

Address: 5 Science Drive 2, Blk MD4, Level 3, Singapore 117545

4 Department of Pharmacology, National University of Singapore

Address: Immunology Programme (National University of Singapore); Centre for Life Sciences Level 3, 28 Medical Drive, Singapore 117456

5 Department of Pathology, National University of Singapore

Address: 10 Kent Ridge Crescent, NUH main building, level 3, Singapore 119260

 # Corresponding author. Address: Massachusetts Institute of Technology, 77 Massachusetts Ave., 16-743, Cambridge, MA 02139. Phone: (617) 258-0260. Fax: (617) 258-0499. E-mail: bevin@mit.edu.

Author contributions

Conceived and designed the experiments: NL, MP, VTKC, BPE. Performed the experiments: NL, MP, TKC, PR, NA. Data analysis/interpretation: NL, MP, LY, KBT, VTKC, BPE. Contributed materials: YY, OK, VTKC, BPE. Wrote the paper: NL, BPE.

Abstract

Influenza viruses account for significant morbidity worldwide. Inflammatory responses, including excessive generation of reactive oxygen and nitrogen species (RONS), mediate lung injury in severe Influenza infections. However, the molecular basis of inflammation-induced lung damage is not fully understood. Here, we studied influenza H1N1 infected cells *in vitro*, as well as H1N1 infected mice, and we monitored molecular and cellular responses over the course of two weeks *in vivo*. We show that influenza induces DNA damage both when cells are directly exposed to virus *in vitro* (measured using the comet assay) and also when cells are exposed to virus in vivo (estimated via γH2AX foci). We show that DNA damage, as well as responses to DNA damage, persist *in vivo* until long after virus has been cleared, at times when there are inflammation associated RONS (measured by xanthine oxidase activity and oxidative products). The frequency of lung epithelial and immune cells with increased γH2AX foci is elevated in vivo, especially for dividing cells (Ki-67 positive) exposed to oxidative stress during tissue regeneration. Additionally, we observed a significant increase in apoptotic cells as well as increased levels of DSB repair proteins Ku70, Ku86 and Rad51 during the regenerative phase. In conclusion, results show that influenza induces DNA both *in vitro* and *in vivo*, and that DNA damage responses are activated, raising the possibility that DNA repair capacity may be a determining factor for tissue recovery and disease outcome.

Keywords: Nuclear foci, Immunofluorescence, Repair deficiency, Acute infection

Abbreviation list:

1, N^6-Etheno-2'-deoxyadenosine (εdA)

1, N^2-Etheno-2'-deoxyguanosine (εdG)

8-hydroxy-deoxyguanosine (8-OH-dG)

8-hydroxyguanosine (8-OH-G)

Alveolar epithelial type II cells (AEII)

Ataxia telangiectasia mutated (ATM)

ATM- and Rad-3 related (ATR)

Base excision repair (BER)

Bronchoalveolar lavage fluid (BALF)

Club cell secretary protein (CCSP)

DNA damage response (DDR)

DNA double strand breaks (DSBs)

DNA-dependent protein kinase catalytic subunit (DNA-PKcs)

Hemagglutinin (HA)

Homologous recombination (HR)

Madin-Darby canine kidney (MDCK)

Multiplicity of infection (MOI)

Non-homologous end joining (NHEJ)

Non-structural protein 1 (NS1)

Phosphatidylinositol-3-kinase-like kinases (PI3K-like kinases)

Pro-Surfactant protein C (Pro-SPC)

Reactive oxygen and nitrogen species (RONS)

DNA single strand breaks (SSBs)

Xanthine oxidase (XO)

Introduction

Influenza A viruses are a group of respiratory pathogens that pose significant health burden worldwide. It has been shown that damage to lung tissue is not only a result of virus-induced cytopathy, but also due to cytotoxic effects of aberrant and excessive inflammation [1,2]. Inflammation-induced reactive oxygen and nitrogen species (RONS) constitute one of the key contributors of pathogenicity in severe influenza A viral infections [3-5]. However, the underlying mechanisms of RONS-induced pathogenesis are not fully understood. RONS exposure leads to DNA lesions, which can promote mutations and cell death [6,7]. Hence, we hypothesize that oxidative DNA damage is induced by influenza-induced inflammation, which may contribute to cytotoxicity *in vivo*.

Inflammation induces many types of base lesions (e.g., 8-hydroxy-deoxyguanosine [8-OH-dG]) and 8-nitroguanosine) [6,8], from which DNA strand breaks can arise via chemical reactions, or via enzymatic processes associated with DNA repair or replication fork breakdown [9,10]. In the presence of DNA damage, cells respond by eliciting DNA damage responses (DDR), which include activation of cell cycle arrest, DNA repair, senescence or cell death, depending on the cell type and severity of DNA damage [11,12]. DDR is orchestrated by many events including post-translational modification of chromatin, which can mediate signal transduction and assembly of repair proteins at the site of DNA strand breaks [13,14]. Phosphorylation of H2AX histones at Ser-139 (γH2AX) is a well-studied example of chromatin modification that occurs following formation of DNA double-strand breaks (DSBs), via the activity of phosphatidylinositol-3-kinase-like kinases (PI3K-like kinases), such as ataxia

telangiectasia mutated (ATM) kinase and DNA-dependent protein kinase catalytic subunit (DNA-PKcs). Signal amplification causes the phosphorylation of H2AX proteins to spread along approximately two megabases around the site of each DSB, to yield γH2AX foci that are visible and quantifiable by immunofluorescence microscopy [15,16]. Interestingly, γH2AX foci can also be triggered by stalled replication fork via ATM- and Rad-3-related (ATR) kinase-dependent phosphorylation. These stalled replication forks can be associated with γH2AX and can breakdown to form physical DSBs [17,18]. Therefore, phosphorylated γH2AX foci indicates the presence of biologically significant DNA damage, and serves as an excellent approach for investigating DSBs and DNA damage induced by replicative stress during influenza infection.

Importantly, the biological importance of γH2AX lies in its involvement in recruiting DNA repair proteins and maintenance of cell cycle arrest in order to facilitate repair of DSBs [19]. Two dominant DSB repair pathways are evolved to counteract the detrimental effects of DSBs, namely non-homologous end joining (NHEJ) and homologous recombination (HR). NHEJ is a rapid joining process that does not require a homologous DNA template. HR is a pathway that enables retrieval of genetic information at the site of the DSB by homology searching, strand invasion and repair synthesis [20]. Both HR and NHEJ require concerted involvement of many DNA repair proteins [19], and defects in DSB repair can contribute to chromosomal breakage and large scale sequence rearrangements that promote cytotoxicity and mutagenesis, respectively [21,22]. Here, we hypothesize that influenza infection induces DNA damage, and that DNA damage responses modulate cytotoxicity and tissue damage in infected mice.

In this study, we used the PR8 mouse model of influenza A (H1N1) virus infection to explore the impact of influenza infection and inflammation on DNA damage and DNA damage responses. By studying chromatin phosphorylation as a measure of DNA damage, we show that the level of DNA damage increases following influenza infection, and we provide data that supports a role for replication fork breakdown as a driver of DNA strand breaks. Importantly, we observed a significant increase in the levels of proteins involved in DSB repair, namely Ku70, Ku86, Rad51 and PCNA, especially during the tissue regenerative phase, suggesting that DNA repair was induced following infection. Together, these studies raise the possibility that DNA damage and DNA repair modulate the severity of influenza-induced cytotoxicity, thereby affecting tissue damage and regeneration, and ultimately disease outcome.

Materials and methods

Cell culture, infection and immunofluorescence

Madin-Darby canine kidney (MDCK) cells were cultured on gelatinized coverslips overnight, and subsequently infected with PR8 influenza at multiplicity of infection (MOI) of one, diluted in 2 mg/mL bovine serum albumin (BSA) (Sigma) and 2 µg/mL tosyl phenylalanyl chloromethyl ketone treated (TPCK-) trypsin (Sigma) in minimum essential medium (MEM) (Invitrogen) for 3, 6, 9, or 12 hours. Non-treated cells were incubated with 2 mg/mL BSA and 2 µg/mL TPCK-trypsin in MEM for 12 hours. Cells were then fixed and incubated with 2 µg/ml mouse anti-γH2AX (Millipore) overnight at 4^0C. Stained cells were then incubated with FITC-conjugated anti-mouse antibody (Santa Cruz), mounted with ProLong Antifade containing DAPI (Invitrogen) and imaged with a Nikon 80i upright microscope under 60x magnification. At least ten images were taken per time point in a blinded fashion. To quantify γH2AX positive cells, images were “blinded” and counted manually for DAPI-positive nuclei. At least 100 cells were counted for each sample, with the exception of three samples for which 82 - 99 cells were quantified. Nuclei harboring 5 or more γH2AX foci were considered positive for γH2AX. Three independent biological replicates were performed for each condition and time-point.

CometChip for high-throughput comet assays of influenza-infected cells

CometChip was fabricated using a polydimethylsiloxane (PDMS, Dow Corning) mold as described previously [23,24]. Briefly, molten 1% normal melting point agarose (Invitrogen) was applied to a sheet of GelBond film (Lonza), and allowed to gel with the PDMS mold on top. Removal of the PDMS mold revealed a ~300 µm thick gel with arrayed microwells. The microwell gel was then clamped between a glass plate and

either a bottomless 24-well or 96-well titer plate (Greiner BioOne) to create the CometChip. Cells were added to each well of the CometChip, and allowed to settle by gravity in complete growth media at 37°C, 5% CO_2. Excess cells were aspirated after 15 min and the bottomless plate was removed in order to capture the arrayed cells in a layer of 1% low melting point agarose (Invitrogen).

After encapsulation in agarose, the bottomless plate was re-aligned to the original position on the CometChip. Wells were infected with 50 µL of PR8 influenza virus at MOI of ~1 in virus medium (0.2% bovine serum albumin, 2 µg/mL TPCK trypsin in minimum essential medium) at 37°C. Negative controls were treated with 50 µL of virus medium under the same conditions. After one hour, the bottomless plate was removed, and all wells were incubated with 0.2% bovine serum albumin and 2 µg/mL TPCK trypsin in Opti-MEM at 37°C. At 3, 6 and 9 h after influenza exposure, at least three influenza virus-infected wells were processed according to either the alkaline or neutral comet assay described in *Supplementary methods and materials*.

Fluorescence imaging and comet analysis

After electrophoresis, alkaline comet and neutral comet gels were neutralized in 0.4 M Tris, pH 7.5 (2 × 15 min) and stained with SYBR Gold (Invitrogen). Images were captured using an automated epifluorescent microscope, and analyzed using custom software written in MATLAB (The Mathworks) [23].

Mouse model and infection

9-12 weeks old C57Bl6Ntac mice (InVivos) were infected with a sublethal dose (12-15 PFU) of H1N1 Influenza A/Puerto Rico/8/34 (PR8) by intratracheal instillation, while

uninfected controls were instilled with same volume of sterile PBS. Procedures were performed in accordance to guidelines and protocols approved by Institutional Animal Care and Use Committee (IACUC). Left lungs were fixed in 10% neutral buffered formalin and paraffin embedded. Alternatively, they were embedded in optimal cutting temperature compound and frozen for histology. Right lungs were frozen in liquid nitrogen or lavaged with 1 ml ice-cold PBS to collect bronchoalveolar lavage fluid (BALF).

Lung homogenization and virus titration

Apical and cardiac lobes were homogenized with 300 µl of PBS with Stainless steel beads (Qiagen) and Qiagen Tissuelyser (max oscillation speed, 2 min, 4^0C). Lung homogenate was spun down at 3000 rcf for 10 min at 4^0C and stored at - 80^0C. Virus titration with MDCK cells was performed based on previous publication [25]. Plaque forming units (PFU) were normalized to protein concentration of lung homogenate estimated with a Bradford assay. *(For more details of plaque assay, please see Supplementary methods and materials)*

Haematoxylin and eosin (H&E) staining and histopathologic analyses

Paraffin-embedded lung sections (5µm) were stained with hematoxylin and eosin (H&E) as described previously with minor modifications [26]. Histopathologic analyses of H&E stained sections were performed by an experienced pathologist. A total of 3-5 sections were analyzed per time-point.

Evaluation of oxidative stress

Lung homogenates processed at various time-points were diluted 100x - 400x with cold PBS. Xanthine oxidase quantification was performed with the diluted lung homogenates using a Xanthine oxidase Fluorometric assay kit (Caymen) based on manufacturer's protocol. To measure oxidative damage to nucleic acids, BALF was collected and centrifuged, and the supernatant was analyzed with a DNA / RNA Oxidative Damage EIA Kit (Caymen) that measures the levels of free 8-OH-dG and 8-hydroxyguanosine (8-OH-G). *(For quantifications of modified DNA bases and etheno adducts, please see Supplementary methods and materials)*

Immunofluorescence

Paraffin sections were boiled in Target retrieval solution (Dako) for 30 min, blocked and permeabilized with 10% Donkey serum in PBS with 0.3% Triton-x 100 for 1 h at room temperature, and then incubated overnight at 4^0C with 20 µg/ml of anti-γH2AX (Cell Signaling), 1 µg/ml of anti-Club cell secretory protein (CCSP; Santa-Cruz), 1 µg/ml of anti-pro-Surfactant protein C (SPC; Santa-Cruz), 1 µg/ml of antibodies against H1N1 non-structural protein 1 (NS1; Santa-Cruz) in staining buffer (5% donkey serum and 0.3% Triton-x 100 in PBS) . Sections were washed and incubated with 5 µg/ml of Alexafluor dyes-conjugated secondary antibodies (Molecular probes) for 1 h at room temperature on the following day, followed by mounting with ProLong gold antifade reagent (Life technologies). To co-stain for Ki-67 and γH2AX, antigen-retrieved lung sections were first incubated with 1 µg/ml anti-Ki-67 (DAKO) for 5 h at room temperature, and incubated with secondary antibodies before tissues were further probed for γH2AX overnight at 4^0C. Cryosections (10 µm) were fixed in 4% PFA for 10 min and stained with 1 µg/ml of anti-CD3 (eBioscience) and 20 µg/ml of anti-γH2AX (Cell Signaling)

based on the protocol described above, except that incubation of primary antibodies were shortened to 1 h at room temperature. *(For Terminal deoxynucleotidyl transferase dUTP nick end labeling (TUNEL) and quantification, please see Supplementary methods and materials)*

Microscopy

All sections were imaged at 20x magnification with Mirax Midi slide scanner or at 40x magnification with Zeiss LSM 700 confocal microscope (Carl Zeiss) at a thickness of 3 µm. Bronchial epithelium were identified by positive CCSP staining and pseudostratified columnar tissue structure. Almost all bronchi and bronchioles were captured from each lung section. In order to collect images for lung parenchyma (CCSP-negative) and pro-SPC positive cells, 10 random regions were captured per lung section. Laser channel for γH2AX was switched off when random fields were selected to prevent bias.

Manual and semi-automated quantification of γH2AX positive cells

Ten images of bronchioles, pro-SPC cells and lung parenchyma were blindly selected and counted for each mouse. To quantify nuclei in the lung parenchyma, DAPI-stained nuclei were counted using Imaris version 7.6.5. At least 1000 cells in the lung parenchyma were counted for each mouse.

Nuclei of bronchial epithelium and pro-SPC cells were counted manually. Bronchioles were first identified by the presence of CCSP staining in the lumen lined by pseudostratified columnar epithelium. All pseudostratified columnar cells in the bronchioles were then counted manually regardless of CCSP expression. At least 400 bronchiolar epithelial cells were counted for each mouse. Pro-SPC-positive cells were

quantified by counting nuclei surrounded by pro-SPC staining. More than 100 cells were counted for most mice, except 5 mice where 53-90 cells were counted as there were fewer pro-SPC positive cells in the captured images. To prevent bias, the fluorescence channel for γH2AX was switched off while manually counting the number of nuclei. Counted nuclei were labelled using the manual spot function on Imaris in order to identify counted cells. For DSB analysis, cells harboring 5 or more foci were considered positive for γH2AX. Cells with pan-nuclear γH2AX were quantified separately.

To determine the relationship between cell division and DSB formation, 15 random images were acquired for lung sections co-stained with Ki-67 and γH2AX. The number of nuclear Ki-67-positive cells in each 0.1 mm^2 lung area, and the proportion of γH2AX-positive cells among the Ki-67 positive population were enumerated manually for each image.

Flow cytometry of BALF cells

BALF cells (1 right lung lavaged with 1 ml PBS) were pelleted and incubated with 1 ml ACK lysis buffer (Life Technologies) for 5 min at room temperature. Cells were then stained with two panels of fluorophore-conjugated antibodies. Panel 1 consisted of anti-CD45-APC, anti-Siglec F-PE, anti-CD11b-PE-Cy7, anti-CD11c-Pacific Blue and anti-GR-1-PerCp Cy5.5. Panel 2 comprised anti-CD45-PE-Cy7, anti-CD3-APC, anti-CD4-PerCP Cy5.5, anti-CD8a-Pacific Blue and anti-CD19-FITC. Cells were stained in PBS with 1% BSA for 30 min at room temperature, and the populations of alveolar macrophages (Siglec F+ / CD11c+), eosinophils (Siglec F+ / CD11c-), neutrophils (SiglecF- / GR1+ / CD11b+), CD8+ T cells (CD3+ / CD8a+) and CD4+T cells (CD3+ /

CD4+) were quantified based on their surface markers [27-29]). All antibodies were purchased from BD Pharmingen, eBiosciences or Miltenyi biotech. Stained cells were analyzed with BD LSRFortessa (BD Bioscience) and FlowJo.

γH2AX staining of BALF cells

BALF cells were spun onto poly-L-Lysine slides with a Cytospin 3 cytocentrifuge (Thermo Scientific), fixed with 4% PFA for 10 min at room temperature, washed thrice with PBS and blocked / permeabilized with blocking solution (3% BSA with 0.1% Triton-X 100 in PBS) for 1 h at room temperature. Cells were incubated with 5 µg/ml of anti-γH2AX (Cell signaling) and 5 µg/ml of anti-F4/80 (Biolegend) in blocking solution for 1 h at room temperature, washed and stained with 10 µg/ml of Alexafluor dyes conjugated secondary antibodies (Molecular probes) for 45 min at room temperature, followed by staining with DAPI for 15 min.

Western blotting

Middle and inferior lobes were homogenized with 2x Laemmli sample buffer with DTT and boiled. Protein concentration was estimated with DC Protein reagent (Biorad) based on manufacturer's protocol and diluted to the same concentration for each batch of mice. Antibodies used included anti-Hemagglutin (HA; Sinobiological Inc.), anti-γH2AX (Millipore), anti-Rad51, anti-Ku86 (Santa Cruz), anti-Proliferating cell nuclear antigen (PCNA; Santa Cruz), anti-Ku70 (Cell Signaling), anti-cleaved capsase 3 (abcam) and anti-β actin (Sigma). Each blot contained samples from different mice, and seven blots were analyzed for each protein. Blots were exposed on film and analyzed using myImageAnalysis version 1.1 (Thermo Scientific). Bands were selected automatically by

myImageAnalysis software using “Auto-Analyze Find Bands” function. Only HA and cleaved caspase 3 bands were selected manually since control samples did not have distinct bands detectable by myImageAnalysis. In this case, the selected band widths were the same for every lane in each blot. Band intensity (volume of band) was quantified and normalized to uninfected controls and the housekeeping β-actin protein.

Statistical analysis

Quantification data were analyzed with Student’s *t* test or Mann-Whitney U test and western blot analyses were performed with Wilcoxon signed ranked test using Graphpad prism unless otherwise stated in the figure legends.

Results

Influenza infection of cultured cells leads to an increase in γH2AX foci.

We first set out to investigate whether influenza infection of cultured cells leads directly to DNA damage. For these studies, MDCK cells were infected with H1N1 virus at a MOI of 1, fixed at the indicated times, and examined by immunofluorescence to detect γH2AX (Fig. 1a). The frequency of cells with significant increased DNA strand breaks was quantified by counting γH2AX-positive cells that harbor 5 or more γH2AX foci. More than twice as many cells were γH2AX-positive as early as 3 hpi, compared to uninfected control. The number of γH2AX-positive cells decreased thereafter, but remained significantly higher than uninfected control even after 12 hpi (Fig. 1b). This result suggests that viral infection induces DNA strand breaks, at least during the early stage of infection.

To learn more about the potential for influenza to induce DNA strand breaks, we performed a comet assay, a method that is well established for directly measuring physical DNA single stranded lesions and DSBs [24,23]. The underlying principle of the comet assay is that damaged DNA migrates more readily when electrophoresed in comparison to undamaged DNA [30]. We first studied DNA single strand breaks (SSBs), abasic sites and alkali-labile sites in MDCK cells using the alkaline comet assay. We observed a similar trend as compared to the γH2AX assay, wherein there is a significantly higher percentage of DNA in the comet tail (percent tail DNA) at 3 hpi compared to uninfected controls (Fig. 1c). Similarly, the neutral comet assay, which detects DSBs, shows that the comet tail length of influenza-infected cells is significantly

higher at 3 hpi compared to uninfected control in each experiment (Fig. 1d), suggesting that DSBs are elevated in cells at least during the early hours of infection. The result that 6 and 9 hpi are not significantly higher than uninfected controls may be explained by repair of damage, as well as the detection limits for the neutral comet assay, which requires a minimum of about 40-50 DSBs for detection [16,31,32]. In contrast, γH2AX foci labeled by immunofluorescence give rise to a signal sufficient for detecting a single DSB [16,33]. Given that analysis of fluorescent γH2AX foci can be applied to study DNA damage in fixed tissues, it is thus used here as an indicator of DNA damage.

3.2.2 Viral load peaks before cellular infiltration.

Influenza pathogenesis has long been known to result from a combination of viral infection and host responses [34]. To learn about the impact of influenza on DNA damage and DDRs, we took advantage of a mouse model wherein C57Bl/6 mice were infected sub-lethally with PR8 virus. In this model, we found that the viral titer was highest at 5 days post infection (dpi), and at 9 dpi, median viral titer was reduced by approximately 100 fold. By 13 dpi, no virus was detected indicating that PR8 had been cleared (Fig. 2a). In parallel, significant weight loss among infected mice began at 5 dpi, reached minimum around 9 dpi, and gradually returned to baseline thereafter, suggesting recovery after viral clearance (Suppl. Fig. 1). In contrast with viral load, which peaked on 5 dpi, whole lung images stained with H&E (Fig. 1b) show that the density of infiltrating cells in the lungs was more pronounced from 9 – 17 dpi, suggesting that lung inflammation did not completely resolve for more than two weeks following infection.

In order to study the kinetics of immune responses, we analyzed the immune cell populations among cells in BALF. BALF cells have been shown to roughly correlate with pathologic changes in the lung interstitium, thereby providing a means of sampling the types of cells present in the lungs [130]. Flow cytometric analysis revealed that total BALF cells increased with time (Suppl. Fig. 2a), among which CD45-positive leukocytes peaked at 9 dpi (Fig. 2c). Further analyses indicates that innate cells involved in oxidative burst (namely infiltrating neutrophils followed by alveolar macrophages), were the dominant cell types on 5 dpi, while CD4+ and CD8a+ T cells of adaptive immunity were more prevalent at 9 dpi (Fig. 2d). Interestingly, eosinophils, which are commonly associated with parasites and allergy [131], were a relatively minor proportion of immune cells, but increased at 13 dpi (Suppl. Fig. 2b). Consistent with previous studies [24, 25], and with histological verification by an experienced pathologist, the flow cytometry shows evidence of a contribution by adaptive immunity later during disease progression (7 - 13 dpi). Interestingly, histological analysis also clearly indicates the presence of regenerating lung epithelial cells during the late time-points (from 13 to 17 dpi, when lymphocytic infiltration was still prominent) (Suppl. Fig. 2c). Taken together, these observations demonstrate that immune responses persist after active viral replication, and through until the onset of tissue regeneration.

Oxidative stress is elevated following infection.

In order to evaluate the kinetics of oxidative stress during influenza infection, we measured the levels of xanthine oxidase (XO) and 8-OH-G, which are a reflection of increased RONS production in the lungs. XO, a superoxide producing enzyme that contributes to tissue damage during influenza infection [5] was significantly increased in

the mouse model on 5, 9, and 13 dpi (Fig. 3a). The highest level of XO was measured at 9 dpi, which corresponded with substantial decline in viral load. In addition, 8-OH-G in cell-free BALF gradually increased after infection, reaching significant levels at 13 dpi (Fig. 3b). 8-OH-G (including 8-OH-dG) could arise from free guanosine being oxidized in the extracellular matrix or from accumulation of 8-OH-G released by dead cells into the extracellular matrix, both suggesting higher oxidative stress. The observations that XO and 8-OH-G are elevated demonstrate that oxidative stress is induced in the lungs after influenza infection, when the viral load is suppressed.

Host responses induce DNA damage in lung epithelium after influenza infection.

Based upon the observation that there is an increase in oxidative stress following influenza infection, we asked if DNA strand breaks occur during the course of infection by quantifying cells that have increased γH2AX. Whole lung lysate was first analyzed for influenza antigen HA and phosphorylated γH2AX by western blot (Fig. 4a). Relative intensities of HA and γH2AX bands were quantified and normalized to β-actin, and the levels of HA and γH2AX relative to uninfected controls is shown in Figure 4b - c. While HA was significantly elevated at 5 - 7 dpi (Fig. 4b), total γH2AX in lung lysate was statistically higher than uninfected controls from 7 dpi to 17 dpi (Fig. 4c), suggesting an induction of DNA damage both during and after the phase of active influenza infection in lung cells.

In order to understand the spatiotemporal relationships among DNA damage, infection and inflammation, we evaluated the frequency of γH2AX-positive cells in specific cell types at various times. First, γH2AX-positive (≥ 5 foci) cells in the

bronchiolar epithelium were quantified as described in the Methods section (Fig. 4d). Results show that induction of γH2AX foci (white arrow) in bronchiolar epithelium was evident by 5 dpi after influenza infection (Fig. 4d). Additionally, the frequency of γH2AX positive bronchial cells was highest at 9 dpi and remained significantly higher than uninfected controls at 13 dpi, when virus has been cleared (Fig. 4e). Examination of alveolar epithelial type II cells (AEII) using antibodies against pro-SPC (Fig. 4f) further showed that despite an increasing trend in DNA damage levels in AEII cells from 5 dpi onwards, the frequency of γH2AX-positive AEII cells was only statistically higher than uninfected controls at 13 dpi when viral clearance had already occurred (Fig. 4g). Together, the induction of γH2AX foci in airway and alveolar cells is consistent with DNA damage in lung epithelium after the phase of active viral infection.

Given that influenza infection *in vitro* causes single- and double-stranded lesions in the DNA of cultured MDCK cells, at least during the early time-point post-infection, we next investigated the extent to which DNA damage occurs in directly infected cells versus uninfected cells *in vivo*. Antibody against the influenza NS1 protein (which is only expressed in infected cells) was used to distinguish between infected and uninfected bystander cells in lung tissues. Results show that γH2AX foci were observed in both NS1+ (infected) and NS1- (uninfected) bronchiolar epithelial cells (Fig. 4h), as well as lung parenchymal cells (Suppl. Fig. 3) at 5 and 9 dpi. While no intracellular NS1 staining was found in lung sections at 13 dpi (consistent with the data in Fig. 2a), there were evidently higher levels of γH2AX-positive cells at 13 dpi compared to uninfected controls. Taken together, the presence of γH2AX foci in NS1-negative cells during viral replication and after viral clearance, suggests that although influenza viruses can directly cause

DNA damage in infected cells, other factors also contribute to DNA damage in uninfected cells during influenza pneumonia *in vivo*.

In addition to the presence of cells with punctate γH2AX, we also observed pan-nuclear staining in cells of infected lungs (orange arrows; Fig. 4d). After infection, cells with pan-nuclear γH2AX co-localized to the same regions as caspase 3 positive cells in successive lung sections (data not shown), suggesting that cells with pan-nuclear γH2AX may be apoptotic. These data are consistent with a previous study showing that γH2AX forms a ring structure in the nuclei of pre-apoptotic cells, followed by global γH2AX distribution in the nuclei during the course of apoptosis [35]. However, it is also possible that some portion of pan-nuclear γH2AX phosphorylation is due to the presence of unrepaired complex DNA lesions, as has been shown previously [36].

DNA damage occurs in immune cell populations.

Immune cells are themselves exposed to RONS generated during inflammation. Hence, we evaluated whether inflammation affects the genomic DNA of immune cells during influenza infection. Lung parenchyma, which was highly infiltrated with immune cells after infection, had significantly more γH2AX positive cells than uninfected lung parenchyma (Fig. 5a), especially at later time points (9 and 13 dpi; Fig. 5b), raising the possibility that immune cells also experience DNA damage.

To learn about DNA damage in different immune cells, we analyzed for co-localization of γH2AX and immune cell type specific markers. Immunofluorescence staining of immune cells demonstrates that γH2AX phosphorylation occurs in various

immune cell populations. For example, we found that among BALF cells positive for γH2AX, many are polymophonuclear cells (Fig. 5c) and F4/80+ macrophages (Fig. 5d). In addition, at 9 dpi, when the frequency of γH2AX positive cells was highest in infiltrated lung parenchyma, many CD3+ T cells in lungs were also stained positive for γH2AX foci (Fig. 5e). Thus, γH2AX foci formation in multiple resident and infiltrating cell populations is consistent with extensive DNA damage in many cell types during the course of disease.

Given that programmed cell death can be a consequence of unrepairable DNA damage, we evaluated the kinetics of apoptosis in whole lungs using TUNEL staining (Suppl. Fig. 4a and 4b) and cleaved caspase 3 by Western blot analysis (Suppl. Fig. 4c and 4d). Results indicate that apoptotic markers peaked at 9 dpi which coincides with the kinetics of induction of γH2AX foci. These results raise the possibility that DNA damage, especially from 5 to 9 dpi, contributes to apoptosis both in infected lung epithelium and in damaged immune cells.

Influenza infection elevates DNA damage in dividing cells.

It is known that the predominant forms of DNA damage generated by endogenous stresses are single-strand lesions, such as base damage, abasic sites and SSBs [37,38]. While DNA strand breaks can arise directly via the cleavage of DNA backbone by RONS, strand breaks can also arise via DNA lesions that stall replication forks and generate physical DSBs during replication fork collapse [39]. Our findings show that the frequencies of γH2AX-positive cells were generally higher during 9 to 13 dpi in lung epithelial cells compared to 5 dpi or uninfected mice. Interestingly, similar

mouse models demonstrate that epithelial cells undergo cell division and replacement following influenza-induced lung injury after ~7 dpi [40,41]. These observations are consistent with the possibility that RONS and DNA synthesis during cell division may work synergistically to cause DNA damage by replication fork breakdown.

To explore the possibility that DNA strand breaks in lungs were promoted by contemporaneous inflammation and cell division during influenza infection, lung sections were co-stained for γH2AX and Ki-67, a cell proliferative marker (Fig. 6a). We first quantified the number of Ki-67 cells in random regions of lung sections and found that, consistent with previous reports, there is an overall increase in Ki-67-positive cells following infection, especially during the later time-points of 9 and 13 dpi (Fig. 6b). We then calculated the frequency of γH2AX-positive cells (≥ 5 foci) among the Ki-67 positive cells, and observed an increase in γH2AX positive cells that are undergoing cell division, especially on 13 dpi (Fig. 6c), suggesting that events that occur after infection accentuate DNA damage among proliferating cells. Taken together, these results reveal that DNA damage is promoted in dividing cells after infection, especially during the tissue regeneration phase, consistent with our hypothesis that replication fork breakdown results from RONS-induced DNA lesions in dividing cells.

Interestingly, ELISA and mass spectrometry analysis of purified genomic DNA showed no elevation in the levels of key damaged bases, including 8-OH-dG, 1, N^6-Etheno-2'-deoxyadenosine (εdA), 1, N^2-Etheno-2'-deoxyguanosine (εdG) and Hypoxanthine (Suppl. Fig. 5a-e). The observation that there is not a change in the steady state levels of base lesions does not preclude the possibility that conditions lead to damaged bases. This is due to the fact that DNA glycosylases efficiently remove

damaged bases as part of the base excision repair (BER) pathway. Thus, induced damage may not exceed the capacity of glycosylases to remove the damage, leading to no overall change in the levels of damaged bases in the genome. Nevertheless, many previous studies show that there can be conditions of imbalanced BER, wherein downstream BER enzymes are unable to keep up with DNA glycosylases [42-44]. This can lead to an increase in the overall levels of SSBs, which can be converted to DSBs if closely opposed or if encountered by a replication fork [45-48]. Indeed the observation that influenza leads to an increase in the levels of single strand lesions *in vitro* (as measured by the alkaline comet assay, Fig. 1c) is consistent with an associated increase in γH2AX foci, suggestive of conversion of SSBs into DSBs.

Influenza infection modulates the levels of DNA repair proteins.

DNA repair processes are an essential defense against DNA damage-induced cell death, and may be important in preventing further tissue injury. We therefore explored the possibility that DNA repair enzyme levels are induced by influenza, with particular focus on proteins involved in DSB repair pathways, NHEJ and HR. We observed that a key NHEJ pathway protein, Ku70, is reduced during active influenza infection (Fig. 7a), reaching statistical significance at 5 and 7 dpi compared to uninfected controls. Ku86 (Ku80 in human cells) is also reduced at 7 dpi in three out of seven mice (Fig. 7a), though no statistical significance is observed. However, following 7 dpi, both Ku70 and Ku86 levels increased, and are significantly higher than uninfected control at 17 dpi (Fig. 7b-c). Although the significance of Ku70 and Ku86 reduction at 5 and 7 dpi is unclear, the observation that these proteins increase during tissue

regeneration (13 – 17 dpi) is consistent with a role for NHEJ in protecting cells against inflammation-induced DSBs during the late recovery phase of infection (17 dpi).

In addition to NHEJ proteins, we interrogated the changes in the levels of Rad51, a protein that is critical for HR. We found that Rad51 is consistently upregulated after infection from 5 to 17 dpi (Fig. 7d and 7e). Concomitantly, there is also an increase in PCNA, which is consistent with an elevation in overall cell proliferation after influenza infection (Fig. 7d and 7f). Rad51 expression increases in human and CHO cells during the S and G2 phases of the cell cycle [49], possibly to facilitate HR activity that repairs DSBs predominantly in the presence of newly synthesized sister chromatids [50,20]. Nevertheless, the levels of Rad51 and PCNA are not always concordant, suggesting that expression of Rad51 may be affected by tissue stress, not just cell proliferation. Overall, the increase in proteins involved in NHEJ and HR during tissue recovery phase may reflect increased DNA repair capacity, which potentially contributes to restoration of lung homeostasis following influenza infection.

Discussion

Severe influenza infection is associated with inflammatory illness, gross lung damage, and in some cases, mortality. In addition to exposure to inflammation-induced RONS, influenza infection has also been shown to more directly elicit oxidative stress [51,52], which is thought to be a key contributor of cytotoxicity. While oxidative damage to DNA has been long associated with malignancies and chronic inflammatory disorders [53,54], the impact of inflammation on DNA is less well understood under acute inflammatory conditions, such as during influenza infection. By analyzing DNA repair foci (as indicated by γH2AX), results here show that there is a significant increase in DNA strand breaks in host cells after influenza infection, both *in vitro* and *in vivo*. Extending upon reports that DNA is damaged during influenza infection *in vitro* [55,56], the studies presented here show that DNA damage not only occurs early in viral infection, but persists until long after the virus has cleared. Additionally, analysis of specific cell types shows that both lung epithelial cells and immune cells suffer DNA damage during the regenerative phase of infection. Indeed, results show that dividing cells are particularly vulnerable to DNA damage, which is consistent with replication fork arrest or breakdown upon encounter with RONS-induced DNA damage (created either directly or as downstream intermediates during excision repair). Results shown here thus suggest a possible role for DNA repair in modulating disease outcome.

Following infection, the process of influenza replication can induce intracellular ROS in host cells [57,58], which could contribute to oxidative damage to the host genome. Indeed, ectopic expression of influenza matrix (M2) protein alone in human lung epithelial cell lines (A549 and H441) is sufficient to elevate intracellular and

mitochondrial reactive oxygen species [51]. While direct induction of ROS by viral infection may be important in the disease process, in this study, we observed that viral replication is kinetically separable from γH2AX foci induction. Indeed, integrated results from measures of inflammatory cell infiltration, RONS induced damage to macromolecules, and molecular responses to DNA damage together call attention to the importance of the immune response in the induction of DNA damage in lung epithelial and infiltrating immune cells.

In the PR8 model of influenza studied here, at times when virus is nearly eliminated (*e.g.*, ~9 dpi and later), we observed concurrent epithelial cell division (Ki-67 positive cells), increased γH2AX foci, highly elevated levels of XO, and an increase in CD8+ T cells. These results show that cell division occurs concurrently with increased RONS produced during inflammation. In addition to RONS secreted by inflammatory cells, host cells may also incur ROS stress due to inflammatory mediators such as TNF-α and granzyme A (secreted by CD8+ T cells) that promote intracellular oxidative stress [59-61]. The coincidence of unresolved inflammation and DNA synthesis may account for the observed increase in DNA damage in dividing lung epithelial cells. Interestingly, we observed an earlier peak in DNA damage levels in bronchiolar epithelial cells (9 dpi) compared to AEII (13 dpi). The recovery of alveolar epithelial cells is slower compared to bronchiolar epithelial club cells during influenza infection [40]. Hence, delayed cell division of AEII cells relative to bronchiolar epithelial cells may explain the delay in the kinetics of γH2AX foci among AEII cells.

Failure to effectively repair DNA damage during inflammation may delay tissue recovery. Indeed, a recent study shows that animals that are deficient in DNA repair have an increased susceptibility to inflammation-induced cytotoxicity in the colon [62]. Analogously, pulmonary inflammation during influenza pneumonia may contribute to a poorer prognosis if damaged DNA is not efficiently repaired. While results shown here point to a role for DNA repair in preventing cytotoxicity caused by RONS-induced fork breakdown in dividing cells, it is also possible that DNA repair plays a role in suppressing RONS-induced toxicity in non-dividing cells. Specifically, complex DNA lesions (sites with two or more DNA lesions in close proximity) can develop into gross chromosomal aberrations, detectable when such cells divide [63]. Following influenza infection, injured lung epithelium was shown to undergo cell proliferation and hyperplasia in the midst of inflammation [64,41]. Hence, the ability to prevent or repair DNA lesions before or during DNA replication can potentially play an important role in determining disease outcome of influenza infection.

In the PR8 mouse model of influenza, we observed dynamic changes in the expression levels of NHEJ proteins. In response to DSBs, Ku70 and Ku86 translocate to the sites of DSBs to form the Ku heterodimeric complex that protects exposed DNA ends and recruits DNA-PKcs for downstream NHEJ processing [65]. Deficiency in Ku can lead to DNA degradation at DSBs and increased frequencies of deletions and translocations [66]. Ku deficiency has also been shown to render cells more sensitive to DNA damage-induced apoptosis [67,68]. Here, results show that the levels of Ku70 and Ku86 are increased during the recovery phase of influenza infection (17 dpi), which is

consistent with a possible role for NHEJ in recovery of lung tissue after influenza infection.

In contrast to NHEJ, HR is relatively error-free DSB repair pathway that is active during S/G2, when sister chromatids are available for participation in repair. Results here show that the levels of Rad51, an essential component of HR, increased during the course of influenza infection. Many *in vitro* studies point to relocalization of Rad51 rather than an increase in protein levels in response to genomic stress. Nevertheless, it remains possible that *in vivo* physiological conditions, such as inflammatory stress, lead to a generalized increase in Rad51 protein levels. Indeed, it has been shown that in fibroblasts, Rad51 overexpression alone induces redistribution of Rad51 as foci in nucleus [69]. More importantly, cells with overexpression of Rad51 are protected from DSBs, chromosome aberrations, and apoptosis when exposed to genotoxic exposures [70,69]. Taken together, the observation that there are increased levels of Rad51 in response to influenza is consistent with the possibility that Rad51 enhances DNA repair capacity, protecting cells from genotoxic stress during tissue regeneration.

Results here demonstrate that T cells possess γH2AX foci in inflamed lungs. It has been shown that T lymphocytes can undergo RAG-dependent DNA cleavage during V(D)J recombination, which leads to transient DSBs and γH2AX foci. However, it is also reported that usually fewer than three γH2AX foci are formed in immature thymocytes, which falls below the criteria for being γH2AX positive (defined as a cells with ≥ 5 foci) [71]. Additionally, V(D)J recombination centers are usually restricted to lymphoid organs, such as bone marrow, thymus, lymph nodes and spleen [72]. Mature

T cells, which are present in the lungs, have not been shown to harbor an increase in γH2AX foci. While it is possible that T cells harbor DNA damage in the inflamed lungs, this damage is consistent with T cells being exposed to high levels of RONS. Additionally, since T cells can undergo clonal expansion in the lungs [24], it is likely that DNA replication forks break down upon encounter with RONS associated SSBs, leading to DSBs. Clearly, future studies are needed to clarify the role of DDR on the function, survival, and clearance of immune cells. Such studies have the potential to provide additional insights into the underlying molecular processes that govern inflammation-induced influenza pathogenesis.

In response to influenza infection, lung tissue becomes heavily infiltrated by immune cells, which outnumber lung epithelial cells during peak inflammation. Rodrigue-Gervais *et al.* have shown that in C57Bl/6 infected with PR8, during peak inflammation, more than 60% of whole lung are leukocytes (CD45 positive), wherein the remainder are CD45 negative cells, which include epithelial, endothelial and mesenchymal cells [73]. Granulocytes and mononuclear cells exposed to PMA, LPS and interferon-γ undergo oxidative burst, and has been shown to cause DNA base damages, γH2AX foci formation, and ATM phosphorylation [74,75]. Thus, normal responses of immune cells to inflammatory conditions are potentially DNA damaging, which may in turn modulate cell fate.

In conclusion, this study shows that DNA damage is induced in cells exposed to influenza both *in vitro* and *in vivo*, and the *in vivo* kinetics are consistent with dual roles for direct induction of DNA damage, as well as DNA damage caused by host inflammatory responses. The observation that there are DDRs during influenza infection

may reflect a more generic phenomenon in infectious diseases that are associated with robust acute inflammatory responses. In this regard, this study forms a framework for future investigation of the clinical significance of DNA damage, not just for influenza infections, but also in the context of other acute infectious diseases, for which the role of DNA repair is increasingly recognized. Finally, inefficient DNA repair has been shown to sensitize cells and tissues to DNA damage, potentiating tissue injury. Given that individuals vary in their DNA repair capacity, this study raises the possibility that DNA repair may play a role in disease susceptibility. Taken together, by addressing a previously understudied area of research, this work opens doors to further investigation into the role of DNA damage and repair during severe influenza, and may allude to novel opportunities for ameliorating severe influenza infection as well as other acute microbial diseases.

Acknowledgements

We thank M.C. Phoon and S. H. Lau for propagating influenza virus and technical assistance. This study was supported by the Singapore National Research Foundation (NRF) and administered by the Singapore-MIT Alliance for Research and Technology. The views expressed herein are solely the responsibility of the authors and do not necessarily represent the official views of NRF.

Conflict of Interest

The authors declare no competing interests.

References:

1. Kobasa D, Jones SM, Shinya K, Kash JC, Copps J, Ebihara H, Hatta Y, Kim JH, Halfmann P, Hatta M, Feldmann F, Alimonti JB, Fernando L, Li Y, Katze MG, Feldmann H, Kawaoka Y (2007) Aberrant innate immune response in lethal infection of macaques with the 1918 influenza virus. Nature 445 (7125):319-323. doi:10.1038/nature05495
2. Walsh KB, Teijaro JR, Wilker PR, Jatzek A, Fremgen DM, Das SC, Watanabe T, Hatta M, Shinya K, Suresh M, Kawaoka Y, Rosen H, Oldstone MB (2011) Suppression of cytokine storm with a sphingosine analog provides protection against pathogenic influenza virus. Proceedings of the National Academy of Sciences of the United States of America 108 (29):12018-12023. doi:10.1073/pnas.1107024108
3. Snelgrove RJ, Edwards L, Rae AJ, Hussell T (2006) An absence of reactive oxygen species improves the resolution of lung influenza infection. European journal of immunology 36 (6):1364-1373. doi:10.1002/eji.200635977
4. Vlahos R, Stambas J, Bozinovski S, Broughton BR, Drummond GR, Selemidis S (2011) Inhibition of Nox2 oxidase activity ameliorates influenza A virus-induced lung inflammation. PLoS pathogens 7 (2):e1001271. doi:10.1371/journal.ppat.1001271
5. Akaike T, Ando M, Oda T, Doi T, Ijiri S, Araki S, Maeda H (1990) Dependence on O2- generation by xanthine oxidase of pathogenesis of influenza virus infection in mice. The Journal of clinical investigation 85 (3):739-745. doi:10.1172/JCI114499
6. Lonkar P, Dedon PC (2011) Reactive species and DNA damage in chronic inflammation: reconciling chemical mechanisms and biological fates. International journal of cancer Journal international du cancer 128 (9):1999-2009. doi:10.1002/ijc.25815
7. Cabon L, Galan-Malo P, Bouharrour A, Delavallee L, Brunelle-Navas MN, Lorenzo HK, Gross A, Susin SA (2012) BID regulates AIF-mediated caspase-independent necroptosis by promoting BAX activation. Cell death and differentiation 19 (2):245-256. doi:10.1038/cdd.2011.91
8. Cooke MS, Evans MD, Dizdaroglu M, Lunec J (2003) Oxidative DNA damage: mechanisms, mutation, and disease. FASEB journal : official publication of the Federation of American Societies for Experimental Biology 17 (10):1195-1214. doi:10.1096/fj.02-0752rev
9. Charbon G, Bjorn L, Mendoza-Chamizo B, Frimodt-Moller J, Lobner-Olesen A (2014) Oxidative DNA damage is instrumental in hyperreplication stress-induced inviability of Escherichia coli. Nucleic acids research 42 (21):13228-13241. doi:10.1093/nar/gku1149
10. Simonelli V, Narciso L, Dogliotti E, Fortini P (2005) Base excision repair intermediates are mutagenic in mammalian cells. Nucleic acids research 33 (14):4404-4411. doi:10.1093/nar/gki749
11. Chen X, Chen J, Gan S, Guan H, Zhou Y, Ouyang Q, Shi J (2013) DNA damage strength modulates a bimodal switch of p53 dynamics for cell-fate control. BMC biology 11:73. doi:10.1186/1741-7007-11-73
12. von Zglinicki T, Saretzki G, Ladhoff J, d'Adda di Fagagna F, Jackson SP (2005) Human cell senescence as a DNA damage response. Mechanisms of ageing and development 126 (1):111-117. doi:10.1016/j.mad.2004.09.034
13. Paull TT, Rogakou EP, Yamazaki V, Kirchgessner CU, Gellert M, Bonner WM (2000) A critical role for histone H2AX in recruitment of repair factors to nuclear foci after DNA damage. Current biology : CB 10 (15):886-895
14. Wang J, Gong Z, Chen J (2011) MDC1 collaborates with TopBP1 in DNA replication checkpoint control. The Journal of cell biology 193 (2):267-273. doi:10.1083/jcb.201010026
15. Rogakou EP, Pilch DR, Orr AH, Ivanova VS, Bonner WM (1998) DNA double-stranded breaks induce histone H2AX phosphorylation on serine 139. The Journal of biological chemistry 273 (10):5858-5868
16. Rothkamm K, Lobrich M (2003) Evidence for a lack of DNA double-strand break repair in human cells exposed to very low x-ray doses. Proceedings of the National Academy of Sciences of the United States of America 100 (9):5057-5062. doi:10.1073/pnas.0830918100

17. Ward IM, Chen J (2001) Histone H2AX is phosphorylated in an ATR-dependent manner in response to replicational stress. The Journal of biological chemistry 276 (51):47759-47762. doi:10.1074/jbc.C100569200
18. Ewald B, Sampath D, Plunkett W (2007) H2AX phosphorylation marks gemcitabine-induced stalled replication forks and their collapse upon S-phase checkpoint abrogation. Molecular cancer therapeutics 6 (4):1239-1248. doi:10.1158/1535-7163.MCT-06-0633
19. Podhorecka M, Skladanowski A, Bozko P (2010) H2AX Phosphorylation: Its Role in DNA Damage Response and Cancer Therapy. Journal of nucleic acids 2010. doi:10.4061/2010/920161
20. Mao Z, Bozzella M, Seluanov A, Gorbunova V (2008) DNA repair by nonhomologous end joining and homologous recombination during cell cycle in human cells. Cell cycle 7 (18):2902-2906
21. Richardson C, Jasin M (2000) Frequent chromosomal translocations induced by DNA double-strand breaks. Nature 405 (6787):697-700. doi:10.1038/35015097
22. Helleday T, Lo J, van Gent DC, Engelward BP (2007) DNA double-strand break repair: from mechanistic understanding to cancer treatment. DNA repair 6 (7):923-935. doi:10.1016/j.dnarep.2007.02.006
23. Wood DK, Weingeist DM, Bhatia SN, Engelward BP (2010) Single cell trapping and DNA damage analysis using microwell arrays. Proceedings of the National Academy of Sciences of the United States of America 107 (22):10008-10013. doi:10.1073/pnas.1004056107
24. Weingeist DM, Ge J, Wood DK, Mutamba JT, Huang Q, Rowland EA, Yaffe MB, Floyd S, Engelward BP (2013) Single-cell microarray enables high-throughput evaluation of DNA double-strand breaks and DNA repair inhibitors. Cell cycle 12 (6):907-915. doi:10.4161/cc.23880
25. Li N, Yin L, Thevenin D, Yamada Y, Limmon G, Chen J, Chow VT, Engelman DM, Engelward BP (2013) Peptide targeting and imaging of damaged lung tissue in influenza-infected mice. Future microbiology 8 (2):257-269. doi:10.2217/fmb.12.134
26. Fischer AH, Jacobson KA, Rose J, Zeller R (2008) Hematoxylin and eosin staining of tissue and cell sections. CSH protocols 2008:pdb prot4986. doi:10.1101/pdb.prot4986
27. Zaynagetdinov R, Sherrill TP, Kendall PL, Segal BH, Weller KP, Tighe RM, Blackwell TS (2013) Identification of myeloid cell subsets in murine lungs using flow cytometry. American journal of respiratory cell and molecular biology 49 (2):180-189. doi:10.1165/rcmb.2012-0366MA
28. Han HaZ, S. (2013) Bronchoalveolar Lavage and Lung Tissue Digestion . . Bio-protocol 3 (16):e859
29. Buchweitz JP, Karmaus PW, Harkema JR, Williams KJ, Kaminski NE (2007) Modulation of airway responses to influenza A/PR/8/34 by Delta9-tetrahydrocannabinol in C57BL/6 mice. The Journal of pharmacology and experimental therapeutics 323 (2):675-683. doi:10.1124/jpet.107.124719
30. Collins AR (2004) The comet assay for DNA damage and repair: principles, applications, and limitations. Molecular biotechnology 26 (3):249-261. doi:10.1385/MB:26:3:249
31. Olive PL, Banath JP (2006) The comet assay: a method to measure DNA damage in individual cells. Nature protocols 1 (1):23-29. doi:10.1038/nprot.2006.5
32. Kawaguchi S, Nakamura T, Yamamoto A, Honda G, Sasaki YF (2010) Is the comet assay a sensitive procedure for detecting genotoxicity? Journal of nucleic acids 2010:541050. doi:10.4061/2010/541050
33. Ismail IH, Wadhra TI, Hammarsten O (2007) An optimized method for detecting gamma-H2AX in blood cells reveals a significant interindividual variation in the gamma-H2AX response among humans. Nucleic acids research 35 (5):e36. doi:10.1093/nar/gkl1169
34. Peiris JS, Hui KP, Yen HL (2010) Host response to influenza virus: protection versus immunopathology. Current opinion in immunology 22 (4):475-481. doi:10.1016/j.coi.2010.06.003
35. Solier S, Pommier Y (2009) The apoptotic ring: a novel entity with phosphorylated histones H2AX and H2B and activated DNA damage response kinases. Cell cycle 8 (12):1853-1859

36. Meyer B, Voss KO, Tobias F, Jakob B, Durante M, Taucher-Scholz G (2013) Clustered DNA damage induces pan-nuclear H2AX phosphorylation mediated by ATM and DNA-PK. Nucleic acids research 41 (12):6109-6118. doi:10.1093/nar/gkt304
37. Lindahl T (1993) Instability and decay of the primary structure of DNA. Nature 362 (6422):709-715. doi:10.1038/362709a0
38. Vilenchik MM, Knudson AG (2003) Endogenous DNA double-strand breaks: production, fidelity of repair, and induction of cancer. Proceedings of the National Academy of Sciences of the United States of America 100 (22):12871-12876. doi:10.1073/pnas.2135498100
39. Harper JV, Anderson JA, O'Neill P (2010) Radiation induced DNA DSBs: Contribution from stalled replication forks? DNA repair 9 (8):907-913. doi:10.1016/j.dnarep.2010.06.002
40. Yin L, Xu S, Cheng J, Zheng D, Limmon GV, Leung NH, Rajapakse JC, Chow VT, Chen J, Yu H (2013) Spatiotemporal quantification of cell dynamics in the lung following influenza virus infection. Journal of biomedical optics 18 (4):046001. doi:10.1117/1.JBO.18.4.046001
41. Zheng D, Limmon GV, Yin L, Leung NH, Yu H, Chow VT, Chen J (2013) A cellular pathway involved in Clara cell to alveolar type II cell differentiation after severe lung injury. PloS one 8 (8):e71028. doi:10.1371/journal.pone.0071028
42. Hofseth LJ, Khan MA, Ambrose M, Nikolayeva O, Xu-Welliver M, Kartalou M, Hussain SP, Roth RB, Zhou X, Mechanic LE, Zurer I, Rotter V, Samson LD, Harris CC (2003) The adaptive imbalance in base excision-repair enzymes generates microsatellite instability in chronic inflammation. The Journal of clinical investigation 112 (12):1887-1894. doi:10.1172/JCI19757
43. Harrison JF, Hollensworth SB, Spitz DR, Copeland WC, Wilson GL, LeDoux SP (2005) Oxidative stress-induced apoptosis in neurons correlates with mitochondrial DNA base excision repair pathway imbalance. Nucleic acids research 33 (14):4660-4671. doi:10.1093/nar/gki759
44. Cabelof DC, Raffoul JJ, Nakamura J, Kapoor D, Abdalla H, Heydari AR (2004) Imbalanced base excision repair in response to folate deficiency is accelerated by polymerase beta haploinsufficiency. The Journal of biological chemistry 279 (35):36504-36513. doi:10.1074/jbc.M405185200
45. Sedletska Y, Radicella JP, Sage E (2013) Replication fork collapse is a major cause of the high mutation frequency at three-base lesion clusters. Nucleic acids research 41 (20):9339-9348. doi:10.1093/nar/gkt731
46. Kozmin SG, Sedletska Y, Reynaud-Angelin A, Gasparutto D, Sage E (2009) The formation of double-strand breaks at multiply damaged sites is driven by the kinetics of excision/incision at base damage in eukaryotic cells. Nucleic acids research 37 (6):1767-1777. doi:10.1093/nar/gkp010
47. Kidane D, Murphy DL, Sweasy JB (2014) Accumulation of abasic sites induces genomic instability in normal human gastric epithelial cells during Helicobacter pylori infection. Oncogenesis 3:e128. doi:10.1038/oncsis.2014.42
48. Ebrahimkhani MR, Daneshmand A, Mazumder A, Allocca M, Calvo JA, Abolhassani N, Jhun I, Muthupalani S, Ayata C, Samson LD (2014) Aag-initiated base excision repair promotes ischemia reperfusion injury in liver, brain, and kidney. Proceedings of the National Academy of Sciences of the United States of America 111 (45):E4878-4886. doi:10.1073/pnas.1413582111
49. Chen F, Nastasi A, Shen Z, Brenneman M, Crissman H, Chen DJ (1997) Cell cycle-dependent protein expression of mammalian homologs of yeast DNA double-strand break repair genes Rad51 and Rad52. Mutation research 384 (3):205-211
50. Wong EA, Capecchi MR (1987) Homologous recombination between coinjected DNA sequences peaks in early to mid-S phase. Molecular and cellular biology 7 (6):2294-2295
51. Lazrak A, Iles KE, Liu G, Noah DL, Noah JW, Matalon S (2009) Influenza virus M2 protein inhibits epithelial sodium channels by increasing reactive oxygen species. FASEB journal : official publication of the Federation of American Societies for Experimental Biology 23 (11):3829-3842. doi:10.1096/fj.09-135590

52. Buffinton GD, Christen S, Peterhans E, Stocker R (1992) Oxidative stress in lungs of mice infected with influenza A virus. Free radical research communications 16 (2):99-110
53. Jackson SP, Bartek J (2009) The DNA-damage response in human biology and disease. Nature 461 (7267):1071-1078. doi:10.1038/nature08467
54. Meira LB, Bugni JM, Green SL, Lee CW, Pang B, Borenshtein D, Rickman BH, Rogers AB, Moroski-Erkul CA, McFaline JL, Schauer DB, Dedon PC, Fox JG, Samson LD (2008) DNA damage induced by chronic inflammation contributes to colon carcinogenesis in mice. The Journal of clinical investigation 118 (7):2516-2525. doi:10.1172/JCI35073
55. Vijaya Lakshmi AN, Ramana MV, Vijayashree B, Ahuja YR, Sharma G (1999) Detection of influenza virus induced DNA damage by comet assay. Mutation research 442 (1):53-58
56. Khanna M, Ray A, Rawall S, Chandna S, Kumar B, Vijayan VK (2010) Detection of influenza virus induced ultrastructural changes and DNA damage. Indian journal of virology : an official organ of Indian Virological Society 21 (1):50-55. doi:10.1007/s13337-010-0004-1
57. Ling JX, Wei F, Li N, Li JL, Chen LJ, Liu YY, Luo F, Xiong HR, Hou W, Yang ZQ (2012) Amelioration of influenza virus-induced reactive oxygen species formation by epigallocatechin gallate derived from green tea. Acta pharmacologica Sinica 33 (12):1533-1541. doi:10.1038/aps.2012.80
58. Lee JS, Hwang HS, Ko EJ, Lee YN, Kwon YM, Kim MC, Kang SM (2014) Immunomodulatory activity of red ginseng against influenza A virus infection. Nutrients 6 (2):517-529. doi:10.3390/nu6020517
59. Wheelhouse NM, Chan YS, Gillies SE, Caldwell H, Ross JA, Harrison DJ, Prost S (2003) TNF-alpha induced DNA damage in primary murine hepatocytes. International journal of molecular medicine 12 (6):889-894
60. Suematsu N, Tsutsui H, Wen J, Kang D, Ikeuchi M, Ide T, Hayashidani S, Shiomi T, Kubota T, Hamasaki N, Takeshita A (2003) Oxidative stress mediates tumor necrosis factor-alpha-induced mitochondrial DNA damage and dysfunction in cardiac myocytes. Circulation 107 (10):1418-1423
61. Martinvalet D, Dykxhoorn DM, Ferrini R, Lieberman J (2008) Granzyme A cleaves a mitochondrial complex I protein to initiate caspase-independent cell death. Cell 133 (4):681-692. doi:10.1016/j.cell.2008.03.032
62. Calvo JA, Meira LB, Lee CY, Moroski-Erkul CA, Abolhassani N, Taghizadeh K, Eichinger LW, Muthupalani S, Nordstrand LM, Klungland A, Samson LD (2012) DNA repair is indispensable for survival after acute inflammation. The Journal of clinical investigation 122 (7):2680-2689. doi:10.1172/JCI63338
63. Asaithamby A, Hu B, Delgado O, Ding LH, Story MD, Minna JD, Shay JW, Chen DJ (2011) Irreparable complex DNA double-strand breaks induce chromosome breakage in organotypic three-dimensional human lung epithelial cell culture. Nucleic acids research 39 (13):5474-5488. doi:10.1093/nar/gkr149
64. Castleman WL, Powe JR, Crawford PC, Gibbs EP, Dubovi EJ, Donis RO, Hanshaw D (2010) Canine H3N8 influenza virus infection in dogs and mice. Veterinary pathology 47 (3):507-517. doi:10.1177/0300985810363718
65. West RB, Yaneva M, Lieber MR (1998) Productive and nonproductive complexes of Ku and DNA-dependent protein kinase at DNA termini. Molecular and cellular biology 18 (10):5908-5920
66. Betermier M, Bertrand P, Lopez BS (2014) Is non-homologous end-joining really an inherently error-prone process? PLoS genetics 10 (1):e1004086. doi:10.1371/journal.pgen.1004086
67. Errami A, Smider V, Rathmell WK, He DM, Hendrickson EA, Zdzienicka MZ, Chu G (1996) Ku86 defines the genetic defect and restores X-ray resistance and V(D)J recombination to complementation group 5 hamster cell mutants. Molecular and cellular biology 16 (4):1519-1526
68. Fattah KR, Ruis BL, Hendrickson EA (2008) Mutations to Ku reveal differences in human somatic cell lines. DNA repair 7 (5):762-774. doi:10.1016/j.dnarep.2008.02.008
69. Raderschall E, Bazarov A, Cao J, Lurz R, Smith A, Mann W, Ropers HH, Sedivy JM, Golub EI, Fritz E, Haaf T (2002) Formation of higher-order nuclear Rad51 structures is functionally linked to p21

expression and protection from DNA damage-induced apoptosis. Journal of cell science 115 (Pt 1):153-164
70. Martin RW, Orelli BJ, Yamazoe M, Minn AJ, Takeda S, Bishop DK (2007) RAD51 up-regulation bypasses BRCA1 function and is a common feature of BRCA1-deficient breast tumors. Cancer research 67 (20):9658-9665. doi:10.1158/0008-5472.CAN-07-0290
71. Chen HT, Bhandoola A, Difilippantonio MJ, Zhu J, Brown MJ, Tai X, Rogakou EP, Brotz TM, Bonner WM, Ried T, Nussenzweig A (2000) Response to RAG-mediated VDJ cleavage by NBS1 and gamma-H2AX. Science 290 (5498):1962-1965
72. Abe M, Hayashida K, Takayama K, Shiku H (1991) V(D)J recombinase activity in primary and secondary murine lymphoid organs: assessment by a PCR assay with extrachromosomal plasmids. International immunology 3 (10):1025-1033
73. Rodrigue-Gervais IG, Labbe K, Dagenais M, Dupaul-Chicoine J, Champagne C, Morizot A, Skeldon A, Brincks EL, Vidal SM, Griffith TS, Saleh M (2014) Cellular inhibitor of apoptosis protein cIAP2 protects against pulmonary tissue necrosis during influenza virus infection to promote host survival. Cell host & microbe 15 (1):23-35. doi:10.1016/j.chom.2013.12.003
74. Tanaka T, Halicka HD, Traganos F, Darzynkiewicz Z (2006) Phosphorylation of histone H2AX on Ser 139 and activation of ATM during oxidative burst in phorbol ester-treated human leukocytes. Cell cycle 5 (22):2671-2675
75. deRojas-Walker T, Tamir S, Ji H, Wishnok JS, Tannenbaum SR (1995) Nitric oxide induces oxidative damage in addition to deamination in macrophage DNA. Chemical research in toxicology 8 (3):473-477

Figure legends (Raw figures in powerpoint 2010 are available upon request)

Fig. 1 H1N1 infection of MDCK cells induces DNA damage and γH2AX foci formation. (a) MDCK cells infected with PR8 virus at MOI 1. γH2AX [green fluorescence (g)] at 3, 6 and 12 h post-infection (hpi) and uninfected controls (Uninf.). (DAPI stained nuclei in blue; b = blue). Images are representative of three independent experiments. Scale bar = 20 µm. (b) Percentages of γH2AX-positive cells (≥ 5 foci per cell). The frequency of γH2AX-positive cells is significantly higher at 3, 9 and 12 hpi compared to uninfected controls. (c) Detection of single strand breaks, abasic sites and alkali sensitive sites using the alkaline comet assay. (d) Detection of double strand breaks with neutral comet assay. (For b - d, results show mean ± SD for three independent experiments; *$p < 0.05$ for paired two-tailed student's *t* test compared to uninfected controls).

Fig. 2 Significant lung inflammation and pathology persist after peak viral load. (a) Viral load peaked at 5 days post-infection (dpi). The number of infectious virus particles (PFU/mg of protein) in lung homogenate was enumerated by a plaque assay. Median viral load peaks at 5 dpi and was reduced by ~10 fold on 7 dpi, and by ~100 fold on 9 dpi (compared to 5 dpi). No viral plaques were detected for uninfected controls or on 13 dpi. (b) Cellular infiltration continues after viral clearance. Whole lung sections were stained with H&E to evaluate the extent of immune cell infiltration. Regions of high cell infiltration are associated with darker purple staining due to higher density of nuclei. Increasing staining density from 5 dpi to 17 dpi is indicative of increased cellular infiltration. Images are representative of 8 - 11 mice. (c) Quantification of total CD45+

leukocyte (results reflect kinetics of immune cell infiltration into the lungs after infection). (d) BALF cell populations are consistent with a transition from innate to adaptive inflammatory responses. BALF cells lavaged from right lungs of mice were stained for cell type specific markers and analyzed by flow cytometry. For abbreviations: AM = alveolar macrophages, Neut = Neutrophils, CD4 T = CD4+ T cells, CD8 T = CD8+ T cells. For 0 dpi, mice were mock instilled with PBS. (For a, c, d, median is indicated by the solid line and each symbol represents one animal; *$p < 0.05$ compared to uninfected controls for two-tailed Mann-Whitney test; n = 6 - 7 mice per time-point).

Fig. 3 Oxidative stress increases following infection. (a) Lung homogenate was analyzed for XO levels. XO levels significantly increased from 5 - 13 dpi compared to uninfected controls, and were highest on 9 dpi. (n = 6 - 7 mice per time-point) (b) Free 8-hydroxyguanosine (8-OH-G) in bronchoalveolar lavage fluid (BALF) is higher post-infection. Median 8-OH-G concentration was significantly higher than controls on 13 dpi. (For a - b, median is indicated by the solid line and each symbol represents one animal; *$p < 0.05$ compared to uninfected controls for two-tailed Mann-Whitney test; n = 3 – 4 per time-point).

Fig. 4 Analysis of γH2AX in lungs during the course of disease. (a) Western analysis of γH2AX and HA in lung lysates shows peak viral load on 5 and 7 dpi and increased γH2AX at 5 - 17 dpi . Results shown are representative of 7 independent experiments. (b) Densitometry of HA by western. (For statistical analysis, n = 7; *$p < 0.05$ for Wilcoxon signed rank test) (c) Densitometry of γH2AX by western. Statistical analysis as

per part b. (d) γH2AX foci formation increased in bronchial epithelial cells after infection. Lung sections were co-stained with club cell secretary protein (CCSP). PR8 infection resulted in increased cells with more than five γH2AX foci (white arrow; magnified in inset) as well as pan-nuclear γH2AX staining (orange arrow). Scale bar = 50 μm. Images are representative of 8 animals per time-point. (e) Number of bronchiolar epithelial cells with ≥ 5 γH2AX foci was highest at 9 dpi. Pseudostratified columnar bronchiolar epithelial cells with ≥ 5 γH2AX foci (γH2AX-positive) and pan-nuclear γH2AX were quantified (see Materials and Methods). The median percentages of γH2AX-positive cells were significantly higher than uninfected controls on 5, 9 and 13 dpi, and highest on 9 dpi. Solid lines indicate median, blue circles show data for cells with ≥ 5 γH2AX foci, and red circles show data for pan-nuclear γH2AX. (For statistical analysis, n = 8 mice per time-point; *$p < 0.05$ compared to uninfected controls for two-tailed Mann-Whitney test) (f) γH2AX formation in cells counter stained for pro-SPC-expressing alveoli type II (AEII) cells. Image is representative of 8 mice per time-point. (g) Frequency of pro-SPC+ cells with more than five γH2AX foci. Statistical analysis as per part e. (h) Increased γH2AX foci formation in both infected and uninfected cells. γH2AX foci were observed among cells positive for NS1 (orange arrows) as well as cells that are not positive for NS1 (white arrows and inset) at 5 dpi and 9 dpi. Scale bar = 20 μm.

Fig. 5 Increased formation of γH2AX foci in immune cells after infection. (a) Increased nuclear-γH2AX in infiltrated lung parenchyma after influenza infection. Infiltrated lung parenchyma (CCSP-negative) were evaluated for γH2AX status (cells with ≥ 5 foci are

designated as being γH2AX positive). Examples of cells that are positive for γH2AX are indicated by the white arrows and are shown in the inset images. Scale bar = 50 µm. Image is representative of 8 mice per time-point. (b) γH2AX-positive cells in lung parenchyma were highest on 9 dpi. The percentages of γH2AX-positive cells and pan-nuclear γH2AX were quantified. Analysis shows *p < 0.05 as compared to uninfected controls according to two-tailed Mann-Whitney test (n = 8 animals per time point). (c) Polymorphonuclear cells (PMNs) and (d) macrophages in bronchoalveolar fluid were γH2AX-positive. γH2AX foci were detected among (c) PMNs that were identified via their multi-lobe nuclei, and (d) macrophages that stained positive with anti-F4/80. (Scale bar shows 10 µm; n = 4 mice per time-point.) (e) γH2AX foci were induced in CD3-positive T cells. Co-staining for CD3 and γH2AX shows that γH2AX foci were induced in T cells. Image is representative of 4 mice on 9 dpi, and 2 mice for uninfected controls.

Fig. 6 Increased DNA damage in proliferating cells after infection. (a) Lung sections were co-stained for γH2AX and Ki-67 at indicated time-points. Examples of Ki-67 positive cells that possess γH2AX foci are indicated by the white arrows and are shown in the inset images. Image is representative of 8 mice per time-point. Scale = 40 µm. (b) Cell proliferation increased after infection. The frequency of Ki-67-positive cells increased in lung tissue after PR8 infection, especially during later time-points of 9 dpi and 13 dpi. (c) Frequency of proliferating cells experiencing DNA damage increased after infection. The percentage of γH2AX positive cells (≥ 5 foci) among total Ki-67 positive cells in lung sections was quantified. (For b – c, solid lines indicate median and each open circle represents an animal. Analysis shows *p < 0.05 as compared to

uninfected controls according to two-tailed Mann-Whitney test (n = 8 animals per time point).

Fig. 7 Western analysis of DNA repair proteins involved in NHEJ and HR. (a) Western analysis of the NHEJ proteins, Ku86 and Ku70. (b-c) Quantification of the levels of Ku86 (b) and Ku70 (c). Levels of Ku86 trend upward and are statistically significantly higher on 17 dpi. Although Ku86 is reduced at 7 dpi in three out of seven mice, the reduction is not statistically significant. Ku70 is at a slightly lower level than controls on 5 and 7 dpi. Similar to Ku86, levels of Ku70 rise and are significantly higher than controls by 17 dpi. (d) Western analysis of Rad51 and PCNA. Representative results are shown from among seven independent experiments. (e-f) Quantification of the levels of Rad51 (e) and PCNA (f). For statistical analysis, $*p < 0.05$ according to the Wilcoxon Sign Rank test. For all results, n = 7 mice per time-point and quantitative data are from seven independent experiments.

Supplementary figures:

Suppl. Fig. 1 Animal weight change profiles. Significant weight changes (*$p < 0.05$) were observed among infected mice compared to uninfected mice (mock infected with PBS) from 5 - 13 dpi. Maximal weight loss was noted on 9 - 10 dpi, and recovery occurred thereafter. Results show mean ± SD for n = 75 mice for infected cohort and 12 mice for control cohort at 0 dpi.

Suppl. Fig. 2 Analysis of influenza-induced pathophysiology. (a) Total live BALF cell counts in right lungs. Right lungs of H1N1-infected or uninfected control mice were lavaged, and cells were quantified using a hemocytometer. Results for individual mice are shown (open circles). Median values are indicated by horizontal bars. (b) Eosinophils (Siglec F+ / CD11c-) were quantified using a Siglec-F-specific antibody in combination with antibodies directed to CD11c. Results for individual mice are shown (open triangles). Median values are indicated by horizontal bars. For a – b, n = 6 - 7 mice at each time-point. (c) Histological analysis of mouse lungs at the indicated times post infection. Infiltration was increased at 5 dpi with a mixture of neutrophils mostly in the airway, and lymphocytes mostly in the alveolar tissue. Magnified inset image for 5 dpi shows neutrophils in bronchioles. Neutrophil infiltration in the airway continued to be prominent at 7 dpi. Magnified inset at 7 dpi shows debris and neutrophils in the airway. A higher level of lymphocyte consolidation was present in the alveolar tissue following 7 dpi, indicating development of pneumonia. Larger region of pneumonia was observed at 9 dpi. Magnified inset at 9 dpi shows lymphocyte consolidation. At 13 and 17 dpi, regenerative tissue was observed, while lymphocyte consolidation was still prominent.

Magnified inset at 13 and 17 dpi shows regenerative tissue. For all images, BR indicates bronchioles, black arrows indicate immune cells, and red arrows indicate regenerating tissue.

Suppl. Fig. 3 Influenza-induced γH2AX foci in both NS1-positive and NS1-negative cells in the lung parenchyma. White arrows indicate representative γH2AX-positive NS1-negative cells (magnified in inset), orange arrows indicates γH2AX-negative NS1-positive cells. Scale bar = 20 μm.

Suppl. Fig. 4 Analysis of influenza-induced apoptosis. (a) Apoptotic cells are detectable by TUNEL staining (green). Ten random fields were quantified for each of 9 - 10 mice per time-point. (b) Percent TUNEL-positive cells peaked on 9 dpi. Quantification of TUNEL-positive cells was performed using Imaris on 10 randomly selected fields. Individual animals are indicated by open circles. Median is indicated by horizontal bar. Statistical analysis shows $*p < 0.05$ compared to uninfected controls according to two-tailed Mann-Whitney. (c) Western analysis shows that cleaved caspase 3 levels are highest on 9 dpi. Results are representative from among seven independent experiments. (d) Quantification of western results show that the levels of cleaved caspase 3 are significantly higher than controls on 7 – 13 dpi. Quantitative data is derived from n = 7 mice for seven independent experiments. $*p < 0.05$ compared to control; Wilcoxon Sign Rank test.

Suppl. Fig. 5 Quantification of damaged bases present in genomic DNA isolated from control and infected lung tissue. (a) ELISA measurement of 8-OH-dG. The levels of 8-OH-dG in nuclear DNA of whole mouse lungs were not significantly different between infected and uninfected mice. Open circles indicate individual mice with three mice per time-point. Medians indicated by horizontal bars. (b) Mass spectrometry quantification of 8-OH-dG, (c) εdA, (d) εdG and (e) hypoxanthine in genomic DNA. Uninf. shows results for mock-infected mice instilled with PBS alone. For 0 dpi, mice were infected with PR8 and euthanized immediately thereafter. (For b-e, results show mean ± SD for n = 3 mice for each time-point; except 3 dpi (n = 2) and 13 dpi (n = 4) for εdA; 3 dpi (n = 2) for 8-OH-dG and εdG; 0, 5, 9 dpi (n = 2) for hypoxanthine.)

Note: Figure created with Microsoft powerpoint 2010

Figure 1

84mm

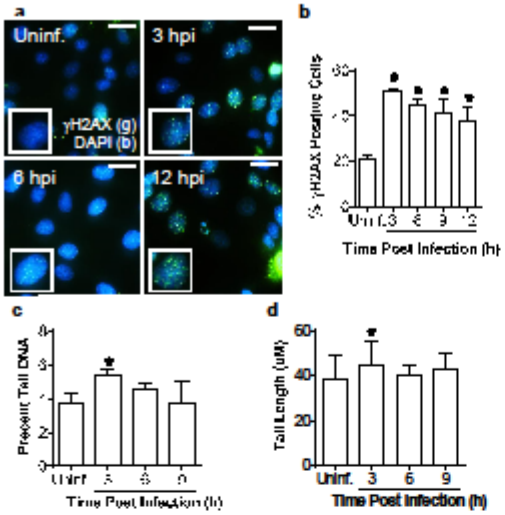

Fig. 1 H1N1 infection of MDCK cells induces DNA damage and γH2AX foci formation. (a) MDCK cells infected with PR8 virus at MOI 1. γH2AX [green fluorescence (g)] at 3, 6 and 12 h post-infection (hpi) and uninfected controls (Uninf.). (DAPI stained nuclei in blue; b = blue). Images are representative of three independent experiments. Scale bar = 20 μm. (b) Percentages of γH2AX-positive cells (≥ 5 foci per cell). The frequency of γH2AX-positive cells is significantly higher at 3, 9 and 12 hpi compared to uninfected controls. (c) Detection of single strand breaks, abasic sites and alkali sensitive sites using the alkaline comet assay. (d) Detection of double strand breaks with neutral comet assay. (For b - d, results show mean ± SD for three independent experiments; $^*p < 0.05$ for paired two-tailed student *t* test compared to uninfected controls).

Note: Figure created with Microsoft powerpoint 2010

Figure 2

129mm

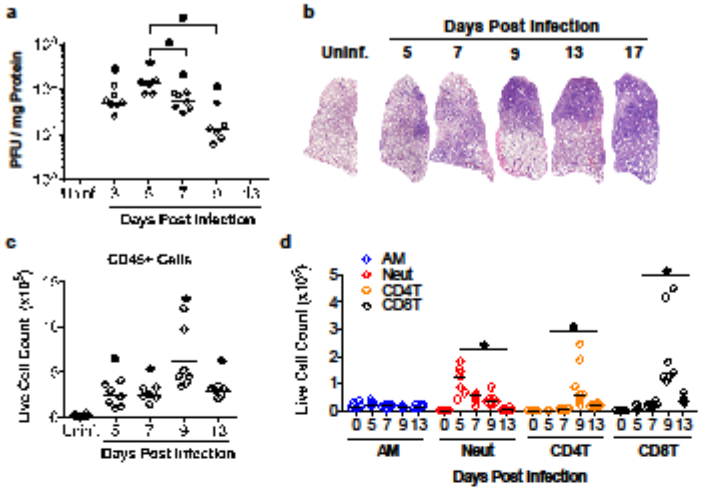

Fig. 2 Significant lung inflammation and pathology persist after peak viral load. (a) Viral load peaked at 5 days post-infection (dpi). The number of infectious virus particles (PFU/mg of protein) in lung homogenate was enumerated by a plaque assay. Median viral load peaks at 5 dpi and was reduced by ~10 fold on 7 dpi, and by ~100 fold on 9 dpi (compared to 5 dpi). No viral plaques were detected for uninfected controls or on 13 dpi. (b) Cellular infiltration continues after viral clearance. Whole lung sections were stained with H&E to evaluate the extent of immune cell infiltration. Regions of high cell infiltration are associated with darker purple staining due to higher density of nuclei. Increasing staining density from 5 dpi to 17 dpi is indicative of increased cellular infiltration. Images are representative of 8 - 11 mice. (c) Quantification of total CD45+ leukocyte (results reflect kinetics of immune cell infiltration into the lungs after infection). (d) BALF cell populations are consistent with a transition from innate to adaptive inflammatory responses. BALF cells lavaged from right lungs of mice were stained for cell type specific markers and analyzed by flow cytometry. For abbreviations: AM = alveolar macrophages, Neut = Neutrophils, CD4 T = CD4+ T cells, CD8 T = CD8+ T cells. For 0 dpi, mice were mock instilled with PBS. (For a, c, d, median is indicated by the solid line and each symbol represents one animal; $^{*}p < 0.05$ compared to uninfected controls for two-tailed Mann-Whitney test; n = 6 - 7 mice per time-point).

Figure 3

84mm

Note: Figure created with Microsoft powerpoint 2010

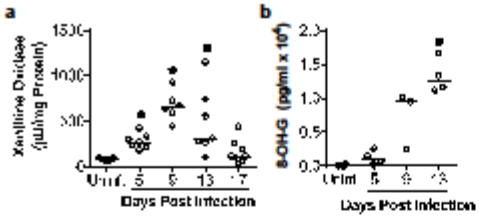

Fig. 3 Oxidative stress increases following infection. (a) Lung homogenate was analyzed for XO levels. XO levels significantly increased from 5 - 13 dpi compared to uninfected controls, and were highest on 9 dpi. (n = 6 - 7 mice per time-point) (b) Free 8-hydroxyguanosine (8-OH-G) in bronchoalveolar lavage fluid (BALF) is higher post-infection. Median 8-OH-G concentration was significantly higher than controls on 13 dpi. (For a - b, median is indicated by the solid line and each symbol represents one animal; $^{*}p < 0.05$ compared to uninfected controls for two-tailed Mann-Whitney test; n = 3 – 4 per time-point).

Figure 4

174mm

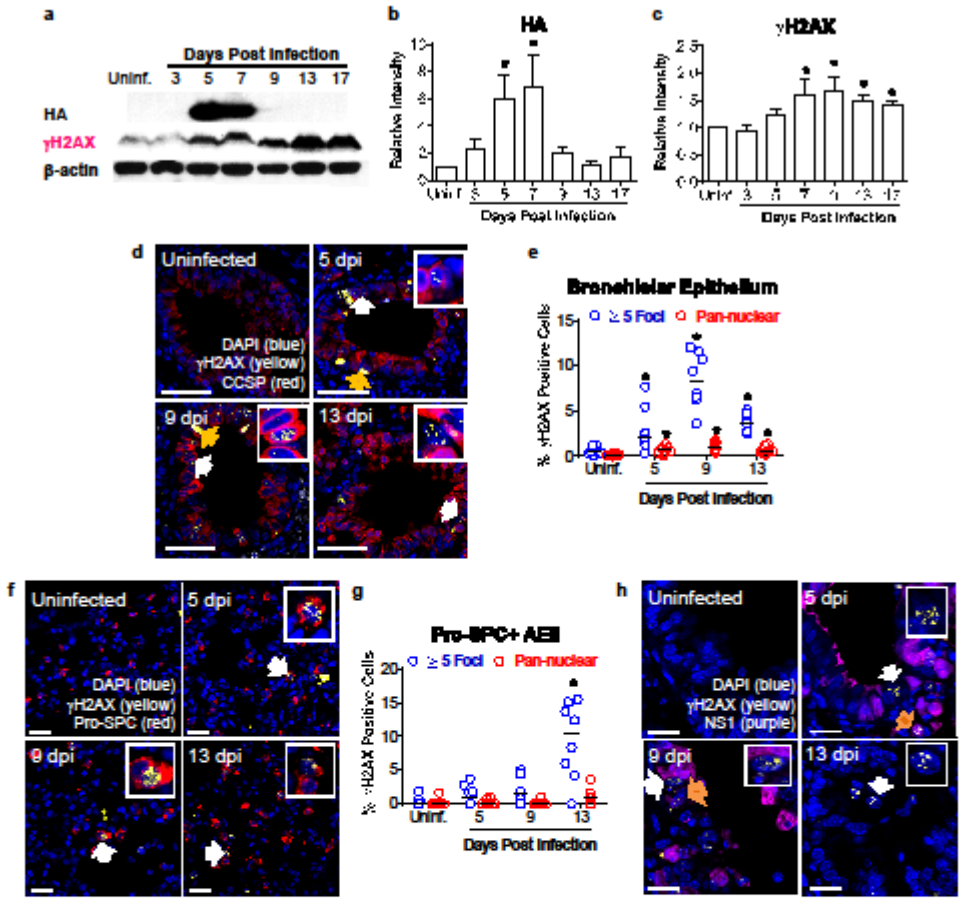

Note: Figure created with Microsoft powerpoint 2010

Figure 5 174mm

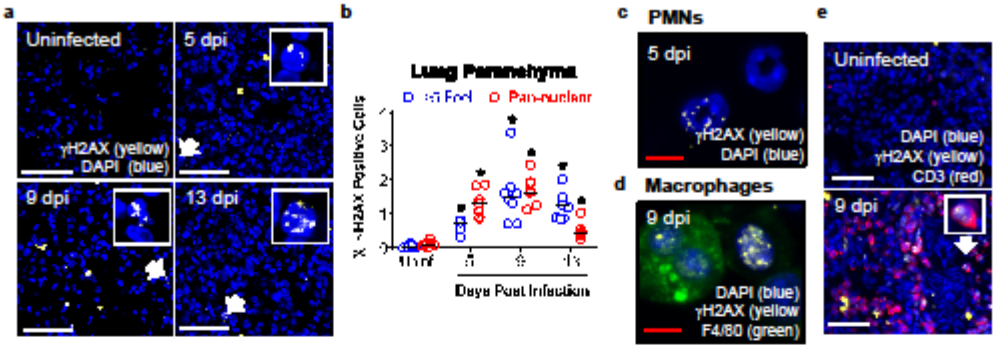

Fig. 5 Increased formation of γH2AX foci in immune cells after infection. (a) Increased nuclear-γH2AX in infiltrated lung parenchyma after influenza infection. Infiltrated lung parenchyma (CCSP-negative) were evaluated for γH2AX status (cells with ≥ 5 foci are designated as being γH2AX positive). Examples of cells that are positive for γH2AX are indicated by the white arrows and are shown in the inset images. Scale bar = 50 μm. Image is representative of 8 mice per time-point. (b) γH2AX-positive cells in lung parenchyma were highest on 9 dpi. The percentages of γH2AX-positive cells and pan-nuclear γH2AX were quantified. Analysis shows $^{*}p < 0.05$ as compared to uninfected controls according to two-tailed Mann-Whitney test (n = 8 animals per time point). (c) Polymorphonuclear cells (PMNs) and (d) macrophages in bronchoalveolar fluid were γH2AX-positive. γH2AX foci were detected among (c) PMNs that were identified via their multi-lobe nuclei, and (d) macrophages that stained positive with anti-F4/80. (Scale bar shows 10 μm; n = 4 mice per time-point.) (e) γH2AX foci were induced in CD3-positive T cells. Co-staining for CD3 and γH2AX shows that γH2AX foci were induced in T cells. Image is representative of 4 mice on 9 dpi, and 2 mice for uninfected controls.

Note: Figure created with Microsoft powerpoint 2010

Figure 6 129mm

Note: Figure created with Microsoft powerpoint 2010

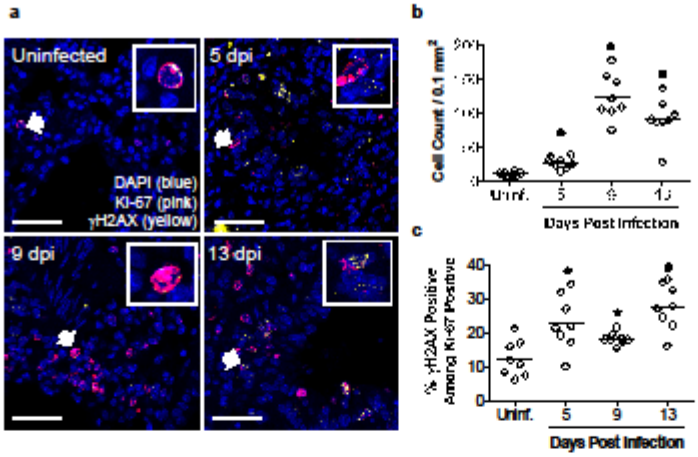

Fig. 6 Increased DNA damage in proliferating cells after infection. (a) Lung sections were co-stained for γH2AX and Ki-67 at indicated time-points. Examples of Ki-67 positive cells that possess γH2AX foci are indicated by the white arrows and are shown in the inset images. Image is representative of 8 mice per time-point. Scale = 40 μm. (b) Cell proliferation increased after infection. The frequency of Ki-67-positive cells increased in lung tissue after PR8 infection, especially during later time-points of 9 dpi and 13 dpi. (c) Frequency of proliferating cells experiencing DNA damage increased after infection. The percentage of γH2AX positive cells (≥ 5 foci) among total Ki-67 positive cells in lung sections was quantified. (For b – c, solid lines indicate median and each open circle represents an animal. Analysis shows $*p < 0.05$ as compared to uninfected controls according to two-tailed Mann-Whitney test (n = 8 animals per time point).

Figure 7 129mm

Note: Figure created with Microsoft powerpoint 2010

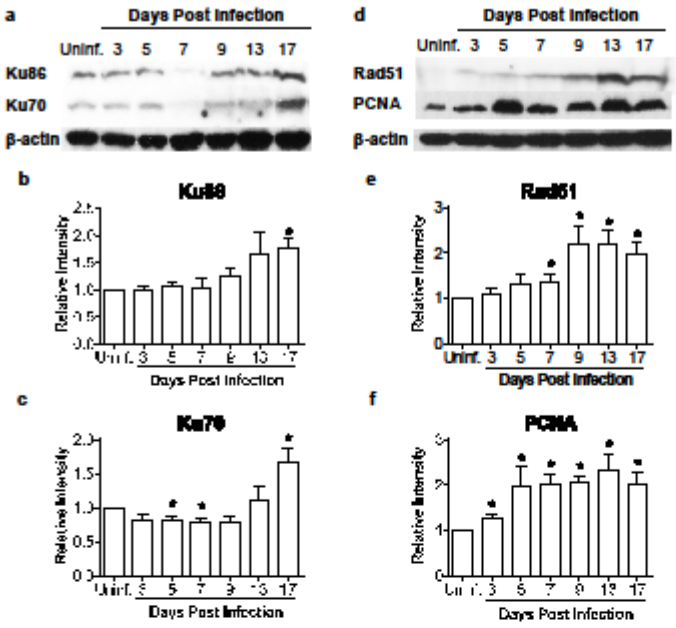

Fig. 7 Western analysis of DNA repair proteins involved in NHEJ and HR. (a) Western analysis of the NHEJ proteins, Ku86 and Ku70. (b-c) Quantification of the levels of Ku86 (b) and Ku70 (c). Levels of Ku86 trend upward and are statistically significantly higher on 17 dpi. Although Ku86 is reduced at 7 dpi in three out of seven mice, the reduction is not statistically significant. Ku70 is at a slightly lower level than controls on 5 and 7 dpi. Similar to Ku86, levels of Ku70 rise and are significantly higher than controls by 17 dpi. (d) Western analysis of Rad51 and PCNA. Representative results are shown from among seven independent experiments. (e-f) Quantification of the levels of Rad51 (e) and PCNA (f). For statistical analysis, $^*p < 0.05$ according to the Wilcoxon Sign Rank test. For all results, n = 7 mice per time-point and quantitative data are from seven independent experiments.